In-plane ultrasonic needle tracking using a fiber-optic hydrophone

Wenfeng Xia[1,a], Jean Martial Mari[1,2], Simeon J. West[3], Yuval Ginsberg[4],
Anna L. David[4], Sebastien Ourselin[5], and Adrien E. Desjardins[1]

[1]*Department of Medical Physics and Biomedical Engineering,*
University College London, Gower Street,
London WC1E 6BT, United Kingdom.

[2]*GePaSud, University of French Polynesia, Faa'a, French Polynesia.*

[3]*Department of Anaesthesia, University College Hospital, London, United Kingdom.*

[4]*Institute for Womens Health, University College London,*
86-96 Chenies Mews, London WC1E 6HX, United Kingdom. and

[5]*Center for Medical Imaging Computing,*
University College London, Gower Street,
London WC1E 6BT, United Kingdom.

[a] Author for correspondance: wenfeng.xia@ucl.ac.uk

Abstract

Purpose: Accurate and efficient guidance of needles to procedural targets is critically important during percutaneous interventional procedures. Ultrasound imaging is widely used for real-time image guidance in a variety of clinical contexts, but with this modality, uncertainties about the location of the needle tip within the image plane lead to significant complications. Whilst several methods have been proposed to improve the visibility of the needle, achieving accuracy and compatibility with current clinical practice is an ongoing challenge. In this paper, we present a method for directly visualizing the needle tip using an integrated fiber optic ultrasound receiver in conjunction with the imaging probe used to acquire B-mode ultrasound images.

Methods: Needle visualization and ultrasound imaging were performed with a clinical ultrasound imaging system. A miniature fiber optic ultrasound hydrophone was integrated into a 20 gauge injection needle tip to receive transmissions from individual transducer elements of the ultrasound imaging probe. The received signals were reconstructed to create an image of the needle tip. Ultrasound B-mode imaging was interleaved with needle tip imaging. A first set of measurements was acquired in water and tissue *ex vivo* with a wide range of insertion angles (15 - 68 degrees) to study the accuracy and sensitivity of the tracking method. A second set was acquired in an *in vivo* swine model, with needle insertions to the brachial plexus. A third set was acquired in an *in vivo* ovine model for fetal interventions, with insertions to different locations within the uterine cavity. Two linear ultrasound imaging probes were used: a 14-5 MHz probe for the first and second sets, and a 9-4 MHz probe for the third.

Results: During insertions in tissue *ex vivo* and *in vivo*, the imaged needle tip had sub-millimeter axial and lateral dimensions. The signal-to-noise (SNR) of the needle tip was found to depend on the insertion angle. With the needle tip in water, the SNR of the needle tip varied with insertion angle, attaining values of 284 at 27 degrees and 501 at 68 degrees. In swine tissue *ex vivo*, the SNR decreased from 80 at 15 degrees to 16 at 61 degrees. In swine tissue *in vivo*, the SNR varied with depth, from 200 at 17.5 mm to 48 at 26 mm, with a constant insertion angle of 40 degrees. In ovine tissue *in vivo*, within the uterine cavity, the SNR varied from 46.4 at 25 mm depth to 18.4 at 32 mm depth, with insertion angles in the range of 26 to 65 degrees.

Conclusion: A fiber optic ultrasound receiver integrated into the needle cannula in combination with single-element transmissions from the imaging probe allows for direct visualization of the needle tip within the ultrasound imaging plane. Visualization of the needle tip was achieved

at depths and insertion angles that are encountered during nerve blocks and fetal interventions. The method presented in this paper has strong potential to improve the safety and efficiency of ultrasound guided needle insertions.

Key words: image guided interventions, ultrasound imaging, medical device tracking, fiber optic hydrophone

I. INTRODUCTION

Precise and efficient guidance of needles to tissue targets in the human body is critical in a wide range of interventional procedures, such as fetal interventions, nerve blocks, central venous catheterisations and tumor biopsies/ablations [1–4]. Ultrasound (US) imaging is widely used for image guidance, but determining the needle tip location with respect to the US imaging plane can be challenging, even for experienced practitioners. One problem is that thin needles readily bend and deviate from the imaging plane so that the locations of their tips may be unknown. A second is that a proximal part of the needle shaft that intersects the imaging plane can be mistaken as the tip. A third is that needles tend to have poor echogenicity during large-angle insertions, particularly when incident US beams are reflected outside the aperture of the imaging probe [5, 6]. In the context of nerve blocks, misinterpreting the position of the needle tip can result in severe complications such as nerve damage [7], local anaesthetic toxicity [8], and pneumothorax [9].

Many methods have been proposed to improve the ultrasonic visibility of medical devices. A prominent method is embodied in echogenic needles, in which surface modifications increase backscattering toward the ultrasound imaging probe. However, the use of echogenic needles can be challenging for insertion angles greater than 50 degrees [10], and they can produce severe image artifacts. Other methods include image processing, shaft vibrations with piezoelectric elements [11], acoustic radiation force imaging [12], and Doppler imaging [13]. Photoacoustic imaging could also be useful for needle visualsation, as it can provide contrast for needles [14] and optical fibers positioned within needles to deliver excitation light [15]. Mechanically constraining the position of the needle relative to the US probe which can be performed with mechanical needle guides [16] and linear bearing devices [17], is not frequently used in clinical practice since re-insertion is required to change to the needle trajectory. Compared with 2D US imaging, 3D US imaging provides improved needle visualization [18–20], but in most clinical fields it is used infrequently due to the high cost and the bulkiness of the probes; moreover, the frequencies are too low for many applications where high spatial resolution is required.

Needle tip positions can also be obtained directly using integrated sensors. Electromagnetic (EM) sensors are notable as they have been widely used in patients in different clinical contexts. A prominent disadvantage of EM sensors is that that their accuracy can be severely degraded by EM field disturbances, including those that arise from commonplace items such as metal tables and instruments [21]. Additionally, they can involve bulky external sensors. Ultrasonic device tracking (UDT) could overcome many of the limitations of EM sensors. With this method, a miniature ultrasound sensor is integrated into the needle. During needle insertions, the sensor receives transmissions from the ultrasound imaging probe located at the surface of the patient. Recently, needle tracking with a two-dimensional array of ultrasound imaging elements was demonstrated. This demonstration by Nikolov *et al.* introduced the concept of reverse beam-forming in the context of 3D imaging, in which the needle tip is effectively imaged using the time-delays associated with one-way ultrasound propagation from elements in the imaging probe to the needle tip. Implementations of this approach with a commercial external ultrasound imaging probe were recently explored [22]. Reception of ultrasound at the device tip can be used to trigger the transmission of a pulse from a source in the device, which can be directly visualized using the external US imaging probe [23]. One of the central requirements for UDT is a sensitive ultrasound sensor that is suitable for integration into medical devices. Piezoelectric ultrasound sensors that are currently available may be suboptimal in this respect, in part due to the challenges with their integration into small diameter needles.

In this study, an ultrasonic tracking system was developed in which a fiber optic hydrophone (FOH) was integrated into a 20 gauge needle. The received signals were reconstructed to obtain an image of the needle tip. Testing was performed with phantoms, and swine tissue *ex vivo* and *in vivo*.

II. MATERIALS AND METHODS

A. Ultrasonic tracking system

Ultrasound imaging was performed with a clinical system (SonixMDP, Analogic Ultrasound, Richmond, BC, Canada) that was operated in research mode. The US imaging probe

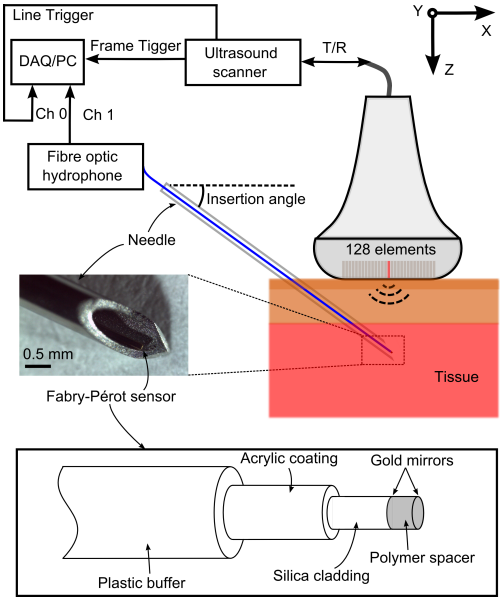

FIG. 1. Schematic of the ultrasonic tracking system.

is a 1D array of 128 transducer elements (L14-5/38, 14-5 MHz Bandwidth, 300 μm pitch, Analogic Ultrasound, Richmond, BC, Canada). A FOH (Precision Acoustics, Dorchester, UK) was inserted into the cannula of a 20 gauge spinal needle (Terumo, Surrey, UK) so that its tip was flush with the bevel surface (Figure 1). The FOH was fixated within the needle cannula with a small quantity of epoxy applied proximal to the distal end face. With the FOH protected by the surrounding cannula, its performance was found to be unchanged after repeated insertions of the needle into soft tissue. Briefly, the hydrophone comprises a thin film Fabry-Pérot interferometer deposited at the distal end face of a single mode fiber (Figure 1). The interferometer is a polymer spacer sandwiched by two gold-coated mirrors. Impinging US waves modulate the spacer thickness; they are detected as modulations in the intensity of back-reflected laser light. The distal end of the FOH is 125 μm which corresponds to the cladding diameter of the fiber. The pressure-voltage sensitivity and the noise equivalent pressure (NEP) are 580 mV/MPa and 15 kPa, respectively; these and other characteristics of the FOH are provided in Ref. [24].

The ultrasound imaging system was controlled with a custom Labview program (National Instruments, Austin, Texas), which served as an interface to low-level libraries for acquisition of B-mode images and transmission of ultrasound pulses for tracking. Acquisitions of B-mode US images were interleaved with tracking transmissions. B-mode US images were acquired

using conventional pulse-echo transmit-receive sequences, with 128 A-scans per image and electronic focusing using an aperture of 64 elements. US transmissions for tracking comprised a sequence of 128 transmissions in which a bipolar electrical pulse excited each transducer element of the imaging probe [Figure 2(a)]. The duration of this excitation pulse was chosen so that its specified center frequency was 10 MHz.

Acquisitions of FOH data were synchronized with the tracking transmissions. Two output triggers were used: a frame trigger corresponding to the start of each B-mode image frame, and a line trigger corresponding to the start of each A-line. The FOH signal acquisition were triggered by the frame trigger, and digitized at 100 MS/s by a DAQ card (USB-5132, National Instrument, Austin, Texas). The line trigger signals were acquired by a second channel of the same DAQ card; once digitized, they were used to parse the FOH data. The data from both channels were sent to the PC in the ultrasound system. A B-mode-tracking image pair was acquired in 20 ms, which could result in a frame rate of 50 Hz. However, to limit the data transfer rate in this study, a delay between the acquisitions of each image pair was imposed, so that the actual frame rate was 1 Hz.

B. Image processing

Real-time data image reconstruction was performed in MATLAB (MathWorks, Natick, Massachusetts) within the Labview programming environment (Figure 1). B-mode ultrasound image processing of RF data included band-pass filtering, envelope detection with the Hilbert transform, and logarithmic transformation prior to display. US tracking images of the needle tip were reconstructed with a Fourier-domain algorithm, the k-Wave MATLAB toolbox [25].

Using the principle of reciprocity, US tracking images were reconstructed with a Fourier-domain algorithm, as implemented with the k-Wave MATLAB toolbox [25]. The algorithm can be understood by analogy with photoacoustic imaging: just as a point source can transmit ultrasound waves that are detected with multiple transducer elements and reconstructed to obtain an image of the source [26], ultrasound waves that are transmitted from multiple transducer elements and detected with the FOH (Figure 2b) can be reconstructed to obtain

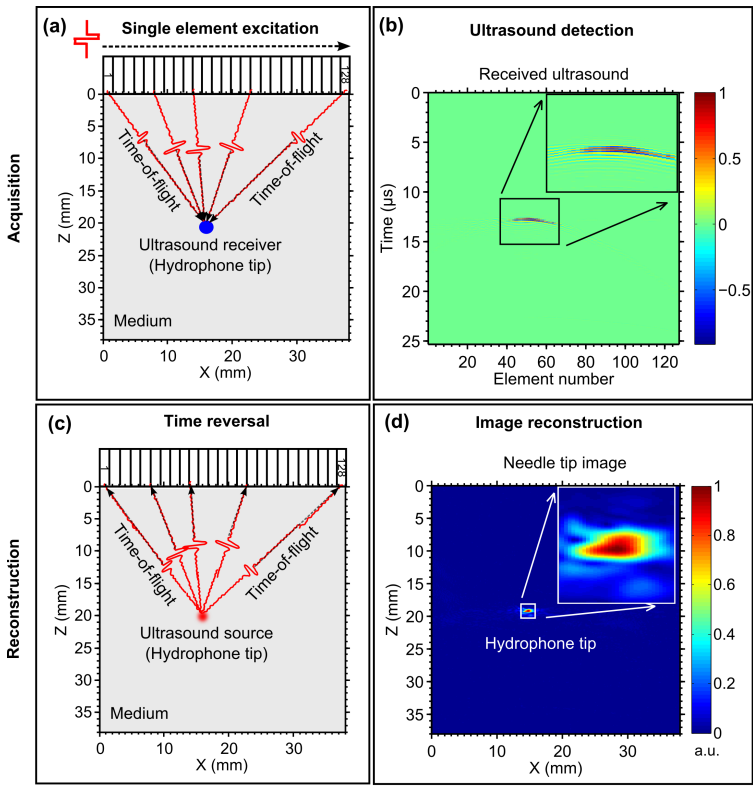

FIG. 2. Schematic illustration of the tracking algorithm, which includes (a) transmission from single transducer elements of the ultrasound imaging probe; (b) detection of ultrasound transmissions by the fiber optic hydrophone; (c, d) Ultrasonic tracking image reconstruction.

an image of the FOH (Figure 2d). Given that the FOH receives ultrasound at the needle tip, the image of the FOH can be interpreted as an image of the needle tip.

C. Experiments

The performance of the US tracking system was measured with needle insertions in two different media. A tank of demineralized water, which was not degassed, was chosen as the first medium, as it allowed for unconstrained motion of the needle. The needle was held rigidly on a linear translation stage and insertions were performed at three angles: 27, 48, and 68 degrees. A swine tissue *ex vivo* that comprised skin, fat, and muscle tissue was chosen as the second medium, with insertions performed at angles of 15, 42 and 61 degrees. With both media, B-mode images and US tracking images were acquired at different depths, when the needle was stationary and the imaging probe was mechanically fixed in position. To measure

the spatial resolution with which the needle tip could be visualized, the axial and lateral profiles of reconstructed needle visualization images were obtained and the corresponding full-width at half-maximum (FWHM) values were calculated. As a measure of sensitivity, the signal-to-noise ratios (SNR) of the needle visualization images were calculated for different insertion angles. To estimate the SNR, a 2 mm x 2 mm area enclosing the hydrophone tip was defined as the signal region, and a 2 mm x 2 mm region outside the signal region was defined as the noise region. The SNR was calculated as the maximum amplitude of the image values in the signal region divided by the standard deviation of the image values in the noise region.

To provide a preliminary indication of the performance of the needle visualization system in clinically realistic conditions, insertions to the brachial plexus of a swine were performed *in vivo* using a linear array, 14-5 MHz ultrasound imaging probe. The needle was inserted at a 40 degree angle and subsequently withdrawn along the same trajectory as the insertion.

A second *in vivo* experiment was performed to evaluate the potential of the system to guide needle insertions in fetal surgery, using a linear array, 9-4 MHz ultrasound imaging probe. Insertions were performed at 2 locations in amniotic fluid, and 5 locations in a fetus: muscle femur, right ventricle, trachea, umbilical vein, stomach. During the experiments, the sheep was maintained under general anesthesia, as previously described [27]. All procedures on animals were conducted in accordance with U.K. Home Office regulations and the Guidance for the Operation of Animals (Scientific Procedures) Act (1986). Ethics approval was provided by the joint animal studies committee of the Royal Veterinary College and the University College London, United Kingdom.

III. RESULTS

With needle insertions performed in water, the tip was clearly apparent in the US tracking images as a single, confined region with high signal amplitude (Figure 3a). At an insertion angle of 68 degrees, this region had a second maximum at a slightly greater depth than the other ($\Delta z \sim 0.25$ mm). Excellent agreement between the tracking and B-mode US images was observed for insertion angles up to 68 degrees. At larger insertion angles, the lack of visibility of the needle in the B-mode US images precluded a direct comparison. The axial and lateral widths of the needle tip region were both consistently less than 1 mm, with values of 0.47

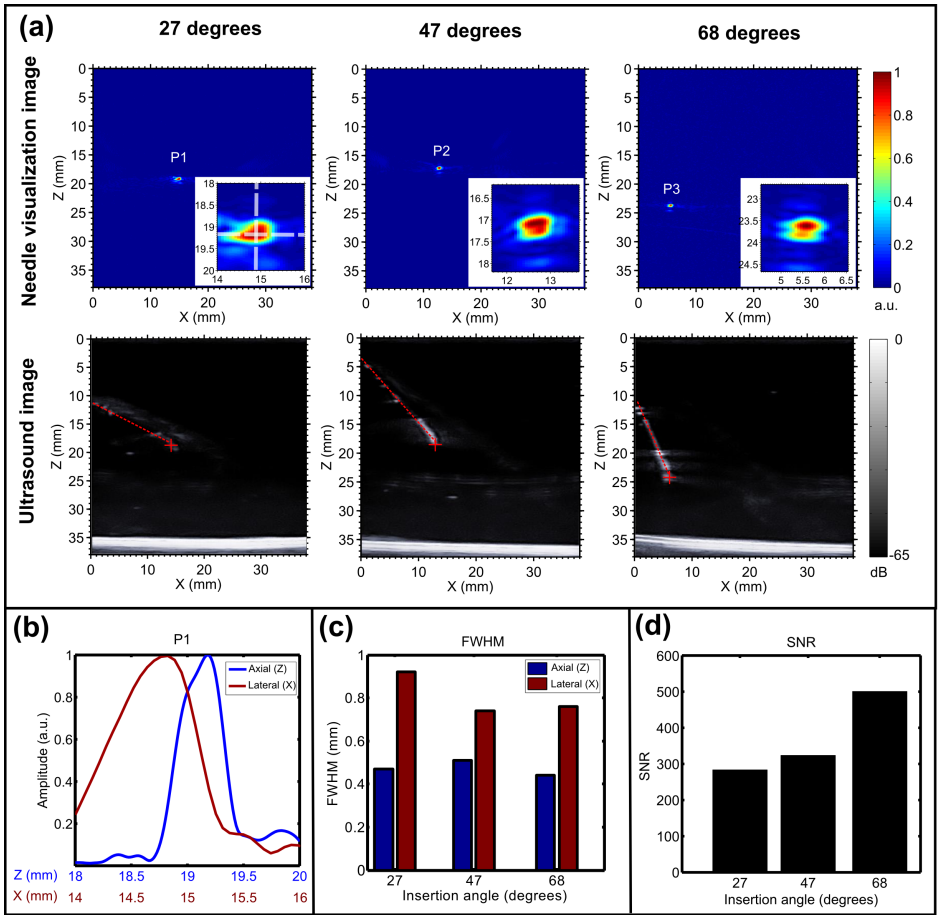

FIG. 3. Needle insertions into water at different angles. Ultrasound images and tracking images are compared in (a). The axial and lateral profiles of the reconstructed needle tip at an insertion angle of 27 degrees are shown in (b). The FWHM and SNR values of the axial and lateral profiles of the imaged needle tip for all insertion angles are compared in (c) and (d), respectively.

mm and 0.92 mm at an insertion angle of 27 degrees (Figure 3b,c). The signal-to-noise ratio (SNR) varied with the needle insertion angle; the highest and lowest values were 501 and 287, which were observed at insertion angles of 68 and 27 degrees, respectively (Figure 3d).

US tracking images obtained with needle insertions into swine tissue *ex vivo* were similar to those in water, albeit with decreased SNRs (Figure 4a; top). At insertion angles of 42 and 61 degrees, the needle tip region of the tracking images comprised two maxima with similar depth separations as that observed with the needle tip in water. Within this heterogeneous medium in which fascial planes, muscle, and adipose tissue were present, the needle had lower visibility on B-mode ultrasound images as it did in water; nonetheless, the insertion angle could still be resolved at angles up to around 61 degrees (Figure 4a; bottom-right).

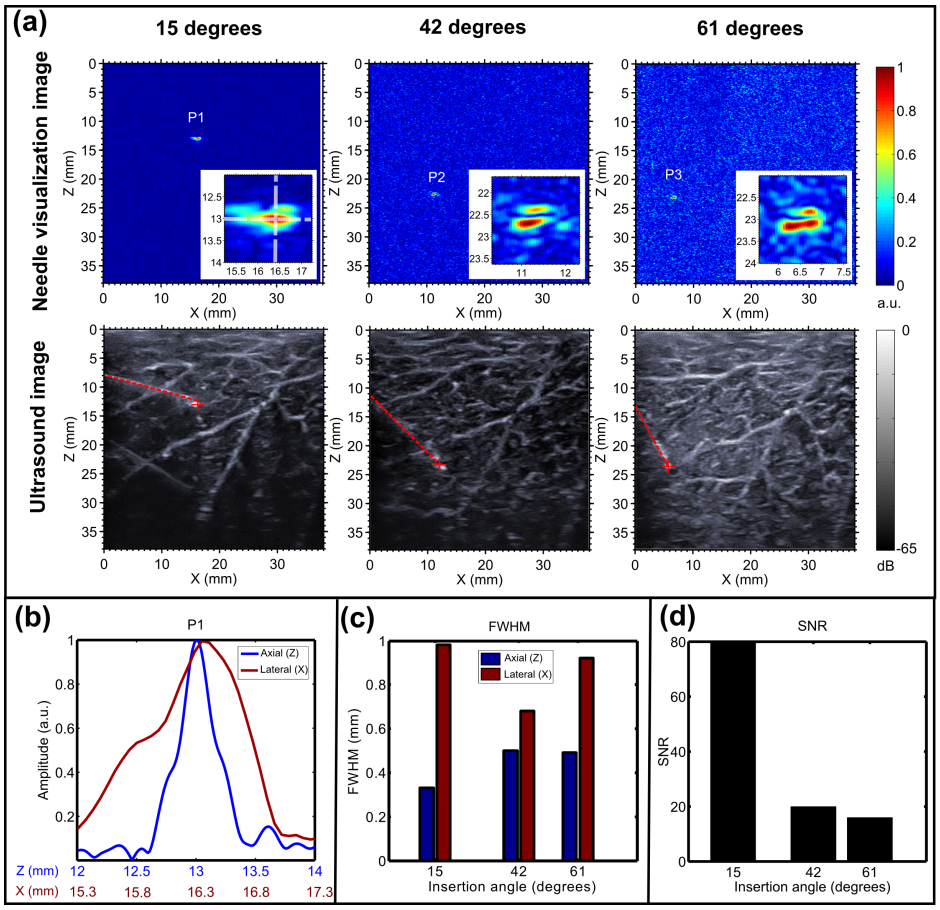

FIG. 4. Insertions into a swine sample *ex vivo* at different angles. Ultrasound and tracking images are compared in (a). The axial and lateral profiles of the reconstructed needle tip with an insertion angle of 15 degrees are plotted in (b). The FWHM and SNR values of the axial and lateral profiles of the imaged needle tip for all insertion angles are compared in (c) and (d), respectively.

The axial and lateral profiles of the needle tip region of the tracking image were similar across insertion angles, they attained values of 0.33 mm and 0.98 mm at an insertion angle of 15 degrees (Figure 4b,c). The SNR varied from a maximum of 80 at 15 degrees, to a minimum of 16 at 61 degrees.

With insertions performed to the brachial plexus of the swine *in vivo*, needle tip visibility was comparable to that of water and significantly higher than that obtained in swine tissue *ex vivo* (Figure 5a). In the B-mode ultrasound images, the brachial plexus manifested as a hyperechoic region beneath the artery/vein pair (Figure 5c). With US tracking images obtained as the needle was retracted to the tissue surface (∼3 mm/s), the axial width of the needle tip region remained nearly constant while the lateral width decreased. At the

brachial plexus, the axial and lateral widths were 0.25 and 1.3 mm, respectively (Figure 5b). The SNR varied from 200 at a depth of 17.5 mm, to 48 at a depth of 26 mm (Figure 5d).

During insertions performed within the uterine cavity of the sheep in vivo, the needle tip reached anatomical target depths in the range of 25 to 41 mm, with insertion angles of 26 to 65 degrees (Table 1). The SNR was above 18 at all anatomical targets, and it reached a maximum of 46.4 in the muscle femur of the fetus (insertion depth/angle: 25 mm/26 degrees). There did not appear to be a consistent relationship between the SNR and the insertion depth or between the SNR and the insertion angle. The FWHM values in the lateral dimension were consistently higher than those in the axial dimension; the former were below 1.69 mm and the latter were below 0.58 mm.

IV. DISCUSSION AND CONCLUSIONS

This study presented a method for in-plane visualization of the needle tip during ultrasound-guided interventions, using a FOH integrated into the needle cannula and image reconstruction of the FOH signals. This method allowed for two ultrasound image types to be obtained: conventional B-mode ultrasound images, and US tracking images that were reconstructed with signals from the FOH. Since the two images were obtained with the same ultrasound imaging probe, they were inherently co-registered, with the same assumed speed-of-sound values used in both cases. However, given that the corresponding reconstruction methods are different, the artifacts resulting from speed-of-sound errors may differ slightly. As a result, the tracking accuracy can be measured by the size of the imaged needle tip. Whilst this study did not address the absolute position accuracy of ultrasonic tracking, it is accurate co-registration between the B-mode ultrasound and the needle visualization images that is of highest clinical importance. Within all four insertion media considered in this study, the axial and lateral sizes of the needle tip in the needle visualization images were very similar to the needle diameter ($\sim$0.91 mm) and the bevel length of the needle ($\sim$1.8 mm), respectively. The accuracy with which the needle tip can be tracked in plane should therefore be sufficient for clinical practice. To directly compare the tracking method used in this study with others, both in terms of spatial accuracy and usability in real clinical contexts, standardized performance metrics and testing conditions are required.

With its small diameter, the FOH was well suited to integration into a needle, and it

could readily be integrated into a wide range of different medical devices. In the context of needle tracking, the FOH has several prominent advantages. One advantage is its broad bandwidth (∼1-50 MHz) [24], so that an FOH can be used for a broad range of clinical ultrasound imaging probes. A second, which stems from its optical design, is its insensitivity to EM field disturbances that afflict EM tracking systems. A third is the simplicity of its design, which lends itself well to high-volume manufacturing and low manufacturing costs that are compatible with single-use devices. Variants of the FOH used in this study, which could include smaller single-mode fibers with 50 or 80 μm cladding diameters, could facilitate integration into small diameter devices. Future studies could focus on more refined designs for integrating the FOH into the needle tip than those considered in this study, which could include a side-arm fitting at the proximal end of the needle to allow for fluid delivery and hydrostatic pressure measurements without removing the FOH. This method was demonstrated on imaging probes with straight linear arrays but it could also be applied to curvilinear probes as well.

The SNR of the US tracking images was sufficient for tracking at steep insertion angles where ultrasound visualization is very challenging. For instance, with the insertion angle of 65 degrees that was included in this study, some echogenic needles are reported to be barely visible [10]. Considering the relatively low attenuation of the ultrasound signals for biological tissues (∼1 dB/cm/MHz) [28] and the high SNR (26.6) achieved at 4.1 cm (Table 1), tracking with the needle tip at depths significantly greater than 4 cm should be feasible with the current system. The lower SNRs obtained with insertions into tissue *ex vivo* may have resulted from changes to the tissue from post-mortem handling; the SNR obtained in tissue *in vivo* was comparable to that of water.

The SNR of the tracking system depends on several parameters that relate to the needle position, the imaging probe, and the characteristics of the medium. These parameters include the needle insertion angle, the coordinates of the needle tip relative to the imaging probe, the frequency bandwidth and the sensitivity of the imaging probe, the acoustic out-of-plane focus of the imaging probe, and the heterogeneity of the tissue. Experimentally, control and measurement of all of these parameters can be very challenging, particularly in an *in vivo* context where there is physiological motion and slippage of the ultrasound imaging probe relative to the tissue surface. Our experience with linear ultrasound imaging probes is that SNR values depend very sensitively on movements of the needle tip in the out-of-plane

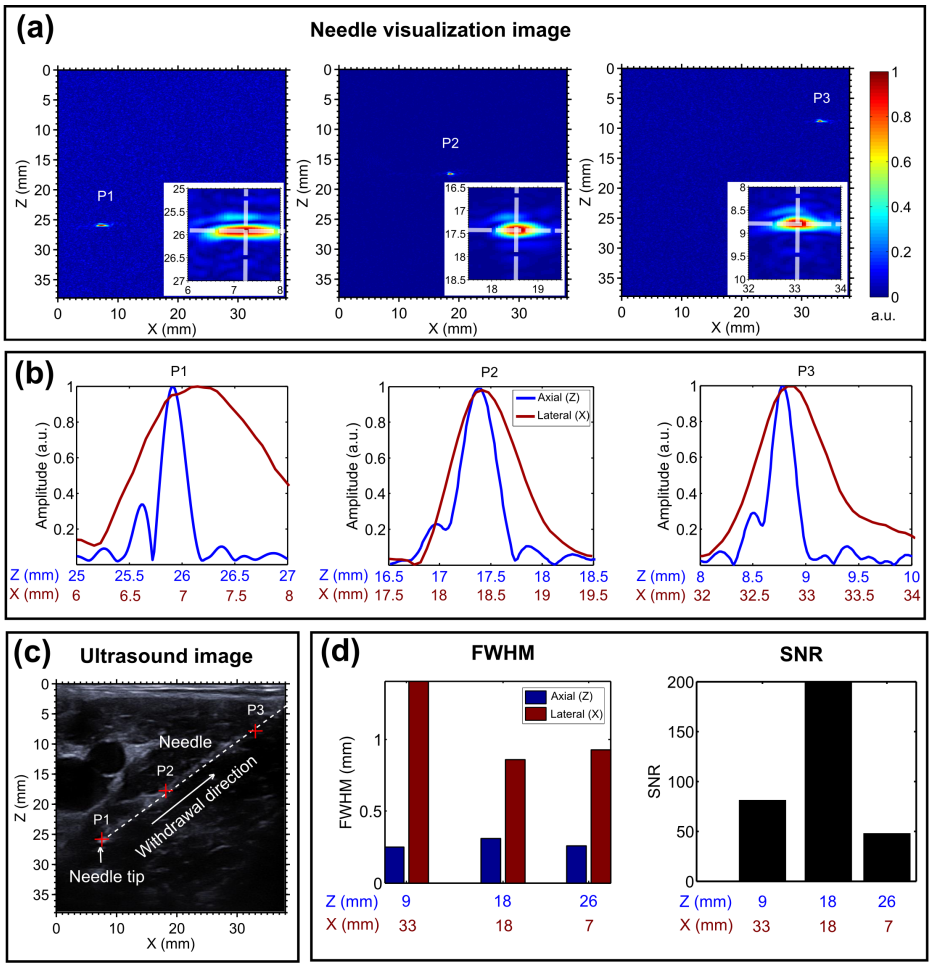

FIG. 5. Needle insertion to the brachial plexus of a swine *in vivo*. Needle tracking (a) and ultrasound images (c) were obtained at several positions as the needle tip was retracted. The axial and lateral profiles of the imaged needle tip at three depths (p1, p2 and p3) are plotted in (b). The SNR and FWHM values of the axial and lateral profiles of the imaged needle tip at all three depths are compared in (d).

direction. The data obtained from the ovine model, which include ranges of depths and insertion angles representative of those observed in clinical practice, provided indications of the variability of the SNR and the FWHM values. One method for increasing the SNR could be to increase the sensitivity of the FOH, for instance by using a Fabry-Pérot interferometer cavity with a curved distal surface to increase the finesse [29]. A second method could be to use coded excitation algorithms, such as those applied in other contexts [30].

The frame rate and image quality of the current system could readily be increased with software optimizations. The choice of a Fourier-domain method for reconstructing FOH

TABLE I. Performance characteristics of the needle tracking images, obtained from needle insertions into fetal sheep within the uterine cavity *in vivo*. The signal strength was measured by the Signal-to-Noise Ratio (SNR); the tracking accuracy, by the Full-Width-at-Half-Maximum (FWHM) values in the axial and lateral dimensions. The standard deviations (S.D.) were calculated from repeated measurements with the needle held manually at fixed positions.

Anatomical location	Insertion depth (mm)	Lateral position (center = 0 mm)	Insertion angle (degrees)	SNR (mean ± S.D.)	FWHM axial (mean ± S.D.) (mm)	FWHM lateral (mean ± S.D.) (mm)
Muscle femur	25	-8.5	26	46.4 ± 6.3	0.58 ± 0.06	1.69 ± 0.06
Right ventricle	31	5.2	65	23.6 ± 2.6	0.52 ± 0.06	1.19 ± 0.14
Trachea	32	4.2	48	18.4 ± 3.8	0.40 ± 0.11	1.07 ± 0.15
Amniotic fluid	33	4.6	56	31.6 ± 6.9	0.39 ± 0.02	0.96 ± 0.06
Umbilical vein	33	1.4	51	27.0 ± 3.2	0.57 ± 0.11	0.92 ± 0.13
Stomach	39	-5.8	49	25.4 ± 9.6	0.45 ± 0.05	0.97 ± 0.06
Amniotic fluid	41	-2.2	57	26.6 ± 5.7	0.43 ± 0.02	0.97 ± 0.05

signals was made on the basis of accuracy; its implementation in Matlab was for computational expediency. Future implementations could include graphics processing units [31] or field programmable gate arrays (FPGAs) [32]. Ultimately, B-mode ultrasound image processing could be informed by the FOH signals. For instance, the US tracking image could be used to automatically select an electronic focus for the B-mode ultrasound images and even to optimize electronic focusing.

Determining both the position of the needle tip when it is outside of the ultrasound imaging plane and the orientation of the needle will be important next steps for the method developed in this study. Out-of-plane information about the position of the needle tip could be particularly valuable for out-of-plane insertions, including navigation to the spinal region when in-plane insertions are not possible. This information could potentially be obtained with ultrasound imaging probe that comprises both a linear array of transducer elements that are focused with an acoustic lens, and additional transducer elements that are unfocused to provide out-of-plane tracking information.

The US tracking method presented in this study is compatible with current clinical prac-

tice, and therefore it has strong potential to increase procedural efficiency and to decrease the risks of complications.

V. ACKNOWLEDGMENTS

This work was supported by an Innovative Engineering for Health award by the Wellcome Trust [WT101957] and the Engineering and Physical Sciences Research Council (EPSRC) [NS/A000027/1], by a Starting Grant from the European Research Council [ERC-2012-StG, Proposal 310970 MOPHIM], and by an EPSRC First Grant [EP/J010952/1]. ALD is supported by the UCL/UCLH NIHR Comprehensive Biomedical Research Centre.

[1] S. P. Emery, J. Kreutzer, F. R. Sherman, K. L. Fujimoto, B. Jaramaz, C. Nikou, K. Tobita, B. B. Keller, "Computer-assisted navigation applied to fetal cardiac intervention," *Int. J. Med. Robotics Comput. Assist. Surg.* **3**, 187–198 (2007).

[2] P. E. Bigeleisen, N. Moayeri, and G. J. Groen, "Extraneural versus intraneural stimulation thresholds during ultrasound-guided supraclavicular block," *Anesthesiology* **110**, 123543 (2009).

[3] A. G. Randolph, D. J. Cook, C. Gonzales, A. Calle, C. G. Pribble, "Ultrasound guidance for placement of central venous catheters: a meta-analysis of the literature," *Critical Care Medicine* **24**(12), 2053–2058 (1996).

[4] M. Ahmed, L. Solbiati, C. L. Brace, D. J. Breen, M. R. Callstrom, J. W. Charboneau, M. Chen, B. I. Choi, T. de Baère, G. D. Dodd III, D. E. Dupuy, D. A. Gervais, D. Gianfelice, A. R. Gillams, F. T. L. Jr, E. Leen, R. Lencioni, P. J. Littrup, T. Livraghi, D. S. Lu, J. P. McGahan, M. Franca Meloni, B. Nikolic, P. L. Pereira, P. Liang, H. Rhim, S. C. Rose, R. Salem, C. T. Sofocleous, S. B. Solomon, M. C. Soulen, M. Tanaka, T. J. Vogl, B. J. Wood, S. N. Goldberg, "Image-guided Tumor Ablation: Standardization of Terminology and Reporting CriteriaA 10-Year Update," *Radiology* **273**(1), 241-260 (2014).

[5] K. Chin, A. Perlas, V. Chan, and R. Brull, "Needle visualization in ultrasound-guided regional anesthesia: challenges and solutions," *Reg. Anesth. pain. Med.* **33**(6), 532–544 (2008).

[6] B. D. Sites, J. M. Neal, and V. Chan, "Ultrasound in reginal anesthesia: where should the "focus" be set?," *Reg. Anesth. pain. Med.* **34**(6), 531–533 (2009).

[7] R. Brull, C. J. L. McCartney, V. W. S. Chan, H. El-Beheiry, "Neurological complications after regional anesthesia: contemporary estimates of risk," *Anesth. Analg.* **104**, 965-974 (2007).

[8] P. J. Zetlaoui, J. Labbe, and D. Benhamou, "Ultrasound guidance for axillary plexus block does not prevent intravascular injection," *Anesthesiology* **108**(4), 761 (2008).

[9] A. Bhatia, J. Lai, V. W. Chan, and R. Brull, "Pneumothorax as a complication of the ultrasound-guided supraclavicular approach for brachial plexus block," *Anesthesia &Analgesia* **111**(3), 817-819 (2010).

[10] S. Hebard, and G. Hocking, "Echogenic technology can improve needle visibility during ultrasound-guided regional anesthesia," *Reg. Anesth. pain. Med.* **36**(2), 185-189 (2011).

[11] S. M. Klein, M. P. Fronheiser, J. Reach, K. C. Nielsen, S. W. Smith, "Piezoelectric vibrating needle and cathether for enhancing ultrasound-guided peripheral nerve blocks," *Anesth. Analg.* **105**, 1858-60 (2007).

[12] V. Rotemberg, M. Palmeri, S. Rosenzweig, S. Grant, D. Macleod, and K. Nightingale, "Acoustic radiation force impulse (ARFI) imaging-based needle visualization," *Ultrason. Imag.* **33**(1), 1-16 (2011).

[13] M. P. Fronheiser, S. F. Idriss, P. D. Wolf, and S. W. Smith, "Vibrating interventional device detection using real-time 3-D color doppler," *IEEE Trans. Ultrason. Ferroelectr. Freq. Control* **55**(6), 1355-1362 (2008).

[14] J. Su, A. Karpiouk, B. Wang and S. Emelianov, "Photoacoustic imaging of clinical metal needles in tissue," *J. Biomed. Opt.* **15**(2) 021309, (2010)

[15] W. Xia, D. I. Nikitichev, J. M. Mari, S. J. West, R. Pratt, A. L. David, S. Ourselin, P. C. Beard, and A. E. Desjardins, "Performance characteristics of an interventional multispectral photoacoustic imaging system for guiding minimally invasive procedures," *J. Biomed. Opt.* **20**(8) 086005, (2015)

[16] C. Kim, D. Chang, D. Petrisor, G. Chirikjian, M. Han, D. Stoianovici, "Ultrasound probe and needle-guide calibration for robotic ultrasound scanning and needle targeting," *IEEE Trans. Biomed. Eng.* **60**(6) 1728-1734, (2013)

[17] V. Stuber, E. M. Suero, T. Hufner, M. Wiewiorski, C. Krettek, M. Citak, "Linear bearing device as a solution for optical navigation of fine needle procedures," *Technology and Health*

Care **18**(4-5) 267-73, (2010).

[18] P. M. Novotny, J. A. Stoll, N. V. Vasilyev, P. J. del Nido, P. E. Dupont, T. E. Zickler, and R. D. Howe, "GPU based real-time instrument tracking with three-dimensional ultrasound," *Med. Im. Anal.* **11** 458-464, (2007).

[19] J. M. Mari, and C. Cachard, "Ultrasonic scanning of straight micro tools in soft biological tissues: Methodology and implementation," *Ultrasonics* **51**(5), 632–638 (2011).

[20] M. Barva, J. M. Mari, M. Uhereik, J. Kybic, J. R. Duhamel, C. Cachard, V. Hlavac, "Parallel integral projection transform for straight electrode localization in 3D ultrasound images," *IEEE Trans. Ultrason. Ferroelectr. Freq. Control* **55**(7), 1559–1569 (2008).

[21] F. Poulin, L. P. Amiot, "Interference during the use of an electromagnetic tracking system under OR conditions," *J. Biomech.* **35** 733-737, (2002)

[22] J. Mung, F. Vignon, and A. Jain, "A non-disruptive technology for robust 3D tool tracking for ultrasound-guided interventions," *Medical Image Computing and Computer-Assisted InterventionMICCAI* 153-160, (2011)

[23] X. Guo, B. Tavakoli, H. Kang, J. U. Kang, R. E. Cummings and E. M. Boctor "Photoacoustic active ultrasound element for catheter tracking," *Proc. of SPIE* **8943** 89435M-1, (2014)

[24] P. Morris, A. Hurrell, A. Shaw, E. Zhang, P. C. Beard, P, "A Fabry-Pérot fiber-optic ultrasonic hydrophone for the simultaneous measurement of temperature and acoustic pressure," *J. Acoust. Soc. Am.* **125**(6) 3611-3622, (2009).

[25] B. E. Treeby, and B. T. Cox "k-Wave: MATLAB toolbox for the simulation and reconstruction of photoacoustic wave fields," *J. Biomed. Opt.* **15**(2), 021314 (2010).

[26] P. C. Beard, "Biomedical photocoustic imaging," *Interface Focus* **1**(4), 602–631 (2011).

[27] A. David, T. Cook, S. Waddington, D. Peebles, M. Nivsarkar, H. Knapton, M. Miah, T. Dahse, D. Noakes, H. Schneider, C. Rodeck, C. Coutelle, M. Themis, "Ultrasound guided percutaneous delivery of adenoviral vectors encoding the beta-galactosidase and human factor IX genes to early gestation fetal sheep in utero," *Human Gene Therapy* **14**, 353–364 (2003).

[28] T. L. Szabo, "Diagnostic ultrasound imaging," *Elsevier Academic Press: London*, (2004).

[29] E. Z. Zhang, P. C. Beard "A miniature all-optical photoacoustic imaging probe," *Proc. of SPIE* **7899**, 78991F (2011).

[30] H. Zhao, L. Y. L. Mo, and S. Gao, "Barker-coded ultrasound color flow imaging: Theoretical and practical design considerations," *IEEE Trans. Ultrason. Ferroelectr. Freq. Control* **54**(2),

319-331 (2007).

[31] J. W. Choe, A. Nikoozadeh, O. Oralkan, and B. T. Khuri-Yakub"GPU-based real-time volumetric ultrasound image reconstruction for a ring array," *IEEE Trans. Med. Imaging* **32**(7), 1258-1264 (2013).

[32] U. Alqasemi, H. Li, A. Aguirre, and Q. Zhu, "FPGA-based reconfigurable processor for ultrafast interlaced ultrasound and photoacoustic imaging," *IEEE Trans. Ultrason. Ferroelectr. Freq. Control* **59**(7), 1344-1353 (2012).